International Journal of Control, Automation, and Systems 22(9) (2024) 2833-2846
http://dx.doi.org/10.1007/s12555-024-0019-9
ISSN:1598-6446 eISSN:2005-4092
http://www.springer.com/12555

Design and Experimental Evaluation of a Leader-follower Robot-assisted System for Femur Fracture Surgery

Fayez H. Alruwaili, Michael P. Clancy, Marzieh S. Saeedi-Hosseiny, Jacob A. Logar, Charalampos Papachristou, Christopher Haydel, Javad Parvizi, Iulian I. Iordachita, and Mohammad H. Abedin-Nasab*

Abstract: In the face of challenges encountered during femur fracture surgery, such as the high rates of malalignment and X-ray exposure to operating personnel, robot-assisted surgery has emerged as an alternative to conventional state-of-the-art surgical methods. This paper introduces the development of a leader-follower robot-assisted system for femur fracture surgery, called Robossis. Robossis comprises a 7-DOF haptic controller and a 6-DOF surgical robot. A control architecture is developed to address the kinematic mismatch and the motion transfer between the haptic controller and the Robossis surgical robot. A motion control pipeline is designed to address the motion transfer and evaluated through experimental testing. The analysis illustrates that the Robossis surgical robot can adhere to the desired trajectory from the haptic controller with an average translational error of 0.32 mm and a rotational error of 0.07°. Additionally, a haptic rendering pipeline is developed to resolve the kinematic mismatch by constraining the haptic controller's (user's hand) movement within the permissible joint limits of the Robossis surgical robot. Lastly, in a cadaveric lab test, the Robossis system was tested during a mock femur fracture surgery. The result shows that the Robossis system can provide an intuitive solution for surgeons to perform femur fracture surgery.

Keywords: Haptic rendering, kinematic mismatch, Robossis, robot-assisted surgery.

1. INTRODUCTION

Robot-assisted surgery has surged in the spotlight of surgical technology due to the demand for increased accuracy and speed needed for the evolution of healthcare [1-3]. This evolution has impacted many targetable areas in need of improvement for ideal surgical outcomes [1-3]. Furthermore, the challenges faced during femur fracture surgery have positioned robot-assisted surgery as a potential alternative to the traditional state-of-the-art clinical techniques [4,5]. These challenges include the substantial amount of force required to reposition and fixate the bone fragments, unacceptably high rates of malalignment and malrotation, and the high X-ray exposure to the operating staff [4,5].

Numerous research studies have been conducted on developing a robot-assisted system for femur fracture surgery, but no system has yet been adequately designed to meet the clinical and mechanical requirements specific to femur fracture surgery applications [4,5]. Particularly, the need for immense force competence, 517 N and 74 N·m [6,7], pinpoint accuracy, Thoresen scoring system as: ±1 cm translational and ±5° rotational alignment [8], and the required surgical-robot workspace.

In previous attempts, Li *et al*. [9] and Kong *et al*. [10] developed teleoperation robot systems for femur fracture alignment based on the Gough-Stewart platform (GSP). Their systems include a bilateral force feedback control framework, a tracking system, and bone-fixing support. However, the main challenge that hinders the developed systems is their practical use in the clinical setting. The small translational and rotational workspaces of the GSP, in combination with the large mechanism size, limit the design's efficacy for femur fracture applications [11]. Furthermore, Westphal *et al*. [12] developed a teleoperation robot system based on the serial-robot mechanism and 6-DOF haptic joystick. A limitation of the robot's serial connection structure is that it is unable to produce the force needed to withstand the large muscle loads around the fe-

Manuscript received January 8, 2024; revised May 31, 2024; accepted June 23, 2024. Recommended by Associate Editor Sangrok Jin under the direction of Senior Editor Kyoung Kwan Ahn. This research was supported by NIH Grant R01EB036365 and NSF Grants 2141099 and 2226489.

Fayez H. Alruwaili, Michael P. Clancy, Jacob A. Logar, and Mohammad H. Abedin-Nasab are with the Biomedical Engineering Department, Rowan University, Glassboro, NJ 08028, USA (e-mails: {alruwa16, clancym1}@rowan.edu, logarj15@students.rowan.edu, abedin@rowan.edu). Marzieh S. Saeedi-Hosseiny is with the Electrical and Computer Engineering Department, Rowan University, Glassboro, NJ 08028, USA (e-mail: saeedi64@rowan.edu). Charalampos Papachristou is with the College of Science & Mathematics, Rowan University, Glassboro, NJ 08028, USA (e-mail: papachristou@rowan.edu). Christopher Haydel is an Orthopedic Trauma Surgery with Virtua Health, Moorestown, NJ 08057, USA (e-mail: chaydel@virtua.org). Javad Parvizi is with Rothman Orthopedic Institute, Thomas Jefferson University Hospital, Philadelphia, Pennsylvania, USA (e-mail: javadparvizi@gmail.com). Iulian I. Iordachita is with the Laboratory for Computational Sensing and Robotics, Johns Hopkins University, Baltimore, MD 21218, USA (e-mail: iordachita@jhu.edu).
* Corresponding author.

mur while maintaining an appropriate size for use in the operating room [4,5].

To address these challenges faced during femur fracture surgeries, Abedin-Nasab *et al*. [13] presented a novel 3-armed 6-DOF parallel robot, called the Robossis surgical robot (RSR). The previous theoretical and experimental analysis demonstrates that the RSR has a rotational workspace 15 times larger than the GSP and can generate the required traction forces up to 1,100 Ns with submillimeter accuracy [14-16]. Furthermore, preclinical cadaver testing demonstrates the feasibility of the RSR to be used in a clinical setting [17,18] .

In this paper, we advance upon the development of the Robossis system by integrating a haptic controller (HC), named the leader, to the RSR, named the follower, to 1) provide an intuitive method to manipulate the RSR and 2) experience haptic feedback.

2. RELATED WORK AND CONTRIBUTION

Intuitive control of kinematically dissimilar leader-follower robotic systems is essential for ensuring safe surgical operation. In these systems, the workspace of the leader manipulator often differs significantly from that of the follower manipulator. The leader is designed to copy the full range of the user's motion input, whereas the follower robot typically has a limited range of motion. As such, when the follower robot reaches its limit during manipulation, the robot may deviate from the intended path and potentially cause additional patient injuries [19].

Developing control strategies to manage kinematic dissimilarity between a leader-follower robotic system is vital for improving the precision and safety of robotic-assisted procedures. To counter this challenge, previous work has introduced varying non-haptic control methods, including soft constraints for joint limits [20], joint limiter approach (JLA) [21], and prescribed performance control (PPC) [22]. The highlighted challenge of these methods is that due to the non-linear kinematics mapping, constraint at the joint level may result in an undesired behavior at the end-effector space.

Furthermore, virtual fixture (VF) is a framework that has been implemented to reshape the task space user input to match the end-effector space of the follower robot. Previous work incorporated VF to address singularity mismatching with repulsion fields [23], incorporating joint limit constraints into cost functions [24], hierarchical optimization frameworks [25], human-centric forbidden-region VF [26], and constraint avoidance-based VF [27]. However, these methods are mainly developed to reshape the task space user input to match a follower robotic system that inherits a serial robotic structure.

However, reshaping the task space user input to match a follower parallel robotic structure is highly complex due to the coupling between the translational and rotational workspace. In parallel robots, the translational and rotational spaces are coupled, meaning that movement in the translational space affects the rotational space and vice versa. This coupling leads to a dynamic and variable forbidden region at the end-effector space with every position and orientation.

Addressing this complexity requires an approach that can dynamically approximate the forbidden region for the follower robot end-effector task space and, therefore, estimate the required haptic information that reshapes the user input motion within these allowable limits. As such, we model the HC end effector by two spherical point clouds to determine the interaction with the dynamic forbidden region and then determine the required haptic information that prevents the user from reaching these locations.

To this end, we propose a novel control architecture that includes 1) a control unit to transfer the motion from the HC to the RSR and 2) a haptic rendering pipeline that addresses the kinematic mismatch between the HC and RSR. The key aspects of our development in this paper are the following:

1) Propose a novel control architecture that integrates the HC with the RSR. The control architecture addresses the challenges of integrating a leader-follower system for kinematically dissimilar robots and motion transfer while maintaining safety and accuracy requirements.
2) Develop a real-time motion control pipeline for the motion transfer from the HC to RSR. We present the integration of the Kalman filter to predict the state of the RSR while maintaining a continuous position, velocity, and acceleration profile. Also, we propose a robust velocity-dependent method that limits the instantaneous velocity of the RSR trajectory to meet the required safety limits.
3) Develop a haptic rendering pipeline to resolve the kinematic mismatch by constraining the HC's (user's hand) movement within the permissible joint limits of the RSR. We model the HC end effector by two spherical point clouds to determine the interaction with the workspace surfaces. The users experience haptic feedback in the directions of the workspace edges to keep the HC inside the RSR workspace limits.

Furthermore, we design a virtual RSR within the Gazebo environment to validate the kinematics of the mechanism and the relationship between users' desired motion and input trajectory. Also, we evaluate the performance of the proposed work via theoretical and experimental testing. Lastly, we conduct a cadaver experiment to demonstrate the feasibility of the Robossis system.

3. ROBOSSIS SYSTEM ARCHITECTURE

The architecture of the Robossis system is described in this section. The Robossis system includes a 7-DOF HC

(Sigma.7, Force Dimension - Switzerland) and the 6-DOF RSR. The sigma.7 HC is a hybrid robot structure based on a delta mechanism providing 3-DOF translational manipulation, a wrist serial mechanism providing 3-DOF rotational manipulation, and a grasping unit for 1-DOF [28,29] (Fig. 1). The RSR is designed based on a 3-armed parallel mechanism where each arm is placed on a moving and fixed ring (Fig. 1). Each arm is actuated with a linear and rotatory actuator (Fig. 1). The Robossis system is designed to meet the clinical requirements of femur fracture surgery, which includes 1) adequately applying the large traction forces/torques, 2) precisely aligning the fractured bone, and 3) manipulating the distal bone fragment during the surgical procedure (in our previous work we provide a clear description of the mechanical and clinical requirement of the RSR [14,17]).

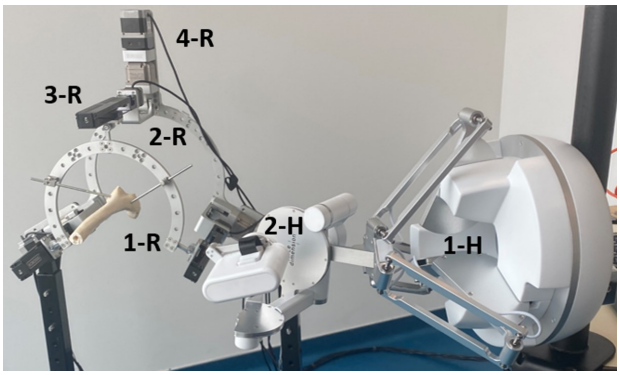

Fig. 1. The leader-follower Robossis system. The HC consists of three identical legs connected in parallel (1-H), attaching between a top triangular fixed base and a mobile end-effector platform and coupled with a hybrid serial arm (2-H). The RSR consists of a moving ring (1-R), a fixed ring (2-R), and three arms, where each arm consists of a linear (3-R) and rotary actuator (4-R).

The entire architecture includes a leader unit, a follower unit, and a communication channel (Fig 2). First, in the leader unit, the user interacts with the HC, and the instantaneous position and velocity are measured from the HC as $\boldsymbol{x}(t)_{\boldsymbol{HC}} \in R^6$ and $\dot{\boldsymbol{x}}(t)_{\boldsymbol{HC}} \in R^6$, respectively. The architecture implements a force restriction, $\boldsymbol{F}(t) \in R^3$ & $\boldsymbol{\tau}(t) \in R^3$, on the HC to reshape the user input motion within these allowable limits of the RSR. These restrictions ensure that the movement of the HC is within the boundaries of the RSR and eliminate any damage to the RSR actuators and structure. Second, motion transfer between the HC and RSR is implemented to map the position and velocity of the users (surgeons) to the end effector of the RSR as $\boldsymbol{x}(t)_{\boldsymbol{RSR}} \in R^6$ and $\dot{\boldsymbol{x}}(t)_{\boldsymbol{RSR}} \in R^6$, respectively.

We implement the Kalman filter to predict the state of the RSR with continuous position, velocity, and acceleration trajectories. Additionally, we implement a robust dynamic scaling method that restricts the input trajectories to the maximum linear and angular velocity (user-defined). Furthermore, we establish a communication channel between the leader and follower units. In the follower unit, the trajectories are unpacked, and the RSR joint velocities are estimated as $\dot{\boldsymbol{q}}(t) \in R^6$. We handle the low-level communication between the control software and the RSR actuators as pulses and directions.

4. INVERSE KINEMATIC ANALYSIS

4.1. Inverse kinematics: Haptic controller

Based on the previous kinematic analysis of the Falcon 3-DOF haptic controller [30-32], a kinematic analysis for the sigma.7 is presented. Fig. 3 presents a top-side view schematic for the three kinematic chains of the sigma.7 HC and its dimension, where i denotes the ith kinematic chain. The origin (center of the stationary platform) is attached to the coordinate frame and labeled point $\boldsymbol{O}$, and

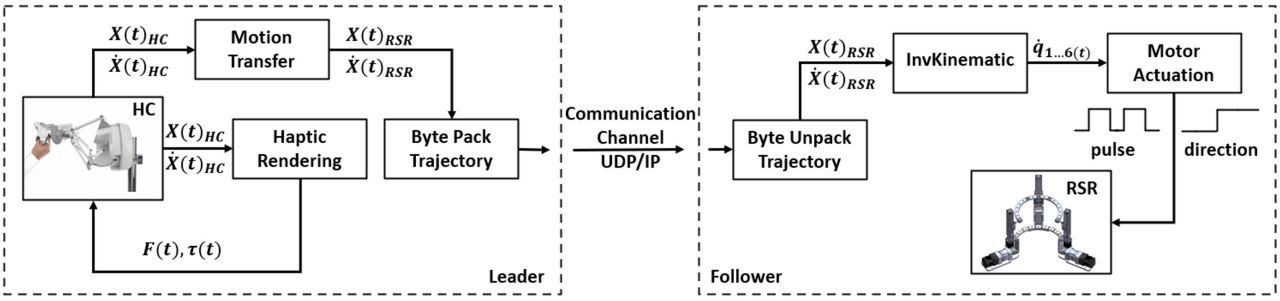

Fig. 2. The proposed Robossis system architecture is illustrated. A leader unit is established where the haptic rendering loop is included to ensure safety for the manipulation of the RSR within its joint space limits. Also, the motion transfer is included that integrates the motion of the user's hand to the RSR for a continuous position, velocity, and acceleration trajectories. A communication channel is established between the leader and follower. In the follower unit, the RSR joint velocities are estimated and the low-level communication with the RSR actuators as pulses and direction are established.

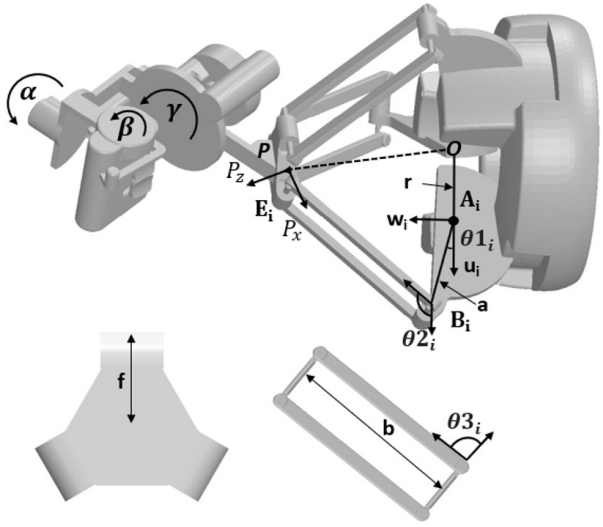

Fig. 3. Kinematic variables of the HC delta mechanism ith arm are shown. The serial mechanism has 3 independent axes of rotation.

point $\boldsymbol{P}$ is defined as the center of the moving platform. The links' lengths are labeled "a" (84 mm) and "b" (175 mm), while the distance between the lowest joint A_i and the center of the stationary platform is indicated by "r" (79 mm). Furthermore, "c" (42 mm) denotes the distance of the highest joint E_i to the center of the moving platform, and "f" (37 mm) denotes the length to the center of the moving platform. A coordinate frame (u_i, v_i, w_i) is defined for each kinematic chain, attached at point $\mathbf{A}_i$.

Equation (1) presents the coordinate transformation of the position of point $\boldsymbol{P}$ in the (u_i, v_i, w_i) coordinate system

$$\begin{bmatrix} Pu_i \\ Pv_i \\ Pw_i \end{bmatrix} = \begin{bmatrix} \cos(\varphi_i) & \sin(\varphi_i) & 0 \\ -\sin(\varphi_i) & \cos(\varphi)i) & 0 \\ 0 & 0 & 1 \end{bmatrix} \times \begin{bmatrix} \cos(\theta) & 0 & \sin(\theta) \\ 0 & 1 & 0 \\ -\sin(\theta) & 0 & \cos(\theta) \end{bmatrix} \begin{bmatrix} Px \\ Py \\ Pz \end{bmatrix} + \begin{bmatrix} -r \\ -s \\ 0 \end{bmatrix}, \tag{1}$$

where θ is 45°, and the angle of the u_i-axis, φ_i, is the distance of the rotation joint from the y-axis. φ_i evaluates as −17°, −137°, and 103°. From Fig. 3, an expression for (Pu_i, Pv_i, Pw_i) is derived as below (2)-(4)

$$Pu_i = a\cos(\theta_{1i}) - c + [b\sin(\theta_{3i})]\cos(\theta_{2i}), \tag{2}$$

$$Pv_i = b\cos(\theta_{3i}) - f, \tag{3}$$

$$Pw_i = a\sin(\theta_{1i}) + [b\sin(\theta_{3i})]\sin(\theta_{2i}). \tag{4}$$

Using (3), a unique solution is determined for the passive joints θ_{3i}. Thus, (2) and (4) can be solved for a solution for the passive and active joints θ_{2i} and θ_{1i}, respectively, as outlined in [30-32].

4.2. Inverse kinematics: Robossis surgical robot

We map the input of the user's hand location and orientation (Fig. 4), $\boldsymbol{P} \in R^6$, as the desired location of the RSR end effector (center of the moving ring ($\boldsymbol{P}$)). Given the position ($P(x,y,z)$) and orientation ($R(\alpha,\beta,\gamma)$) of the endpoint effector ($\boldsymbol{P}$), the length of the linear actuator (d_i) and the rotation of the active joint (θ_i) are computed. Referring to Fig. 4, $\boldsymbol{a_i}$ and $\boldsymbol{b_i}$ epresent OA_i and PB_i, respectively.

Denoting the $\boldsymbol{a_i}$ and $\boldsymbol{b_i}$ position vector in frame {A}, it can be concluded from the structure that

$$\boldsymbol{r_i} - \boldsymbol{a_i} = \boldsymbol{p} + \boldsymbol{b_i} - \boldsymbol{a_i}, \tag{5}$$

where the left-hand side is the length vector of the linear actuator ($\boldsymbol{d_i}$). Simplifying and using Euclidean norm, d_i can be expressed as

$$d_i = \sqrt{(x-x_i)^2 + (y-y_i)^2 + (z-z_i)^2}, \tag{6}$$

where

$$\begin{cases} x_i = -h(\cos(\gamma_i)R_{11} + \sin(\gamma_i)R_{12}) + g\cos(\gamma_i), \\ y_i = -h(\cos(\gamma_i)R_{21} + \sin(\gamma_i)R_{22}) + g\sin(\gamma_i), \\ z_i = -h(\cos(\gamma_i)R_{31} + \sin(\gamma_i)R_{32}), \end{cases} \tag{7}$$

where R is the rotation matrix from {B} to {A}, using Euler angles (X-Y-Z). Also, g and h are the radii of the fixed and moving platforms, respectively, and γ_i is the location of each of the ith arms on the moving platform and denoted as −30°, 90°, and 210°. Thus, the active (θ_i) and passive

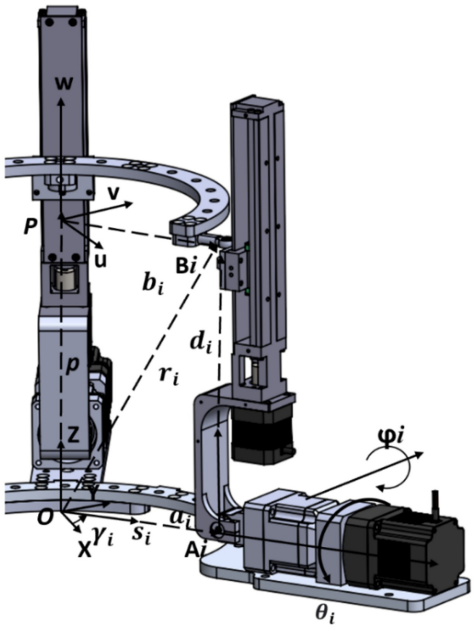

Fig. 4. Kinematic variables of the ith arm of the RSR are shown. d_i is the linear actuator length, θ_i is the active rotation, followed by the passive ψ_i rotation.

(ψ_i) are expressed in (8) and (9) as

$$\theta_i = \sin^{-1}\left(\frac{\sin(\gamma_i)*(x-x_i)-\cos(\gamma_i)*(y-y_i)}{d_i\cos*(\psi_i)}\right), \tag{8}$$

$$\psi_i = \sin^{-1}\left(\frac{\cos(\gamma_i)*(x-x_i)+\sin(\gamma_i)*(y-y_i)}{d_i}\right). \tag{9}$$

Physical constraints, including the length of linear actuators (±70 mm), and spherical joints (±25°), are imposed to determine the allowable translational and rotational workspace of the RSR structure.

4.3. Kinematic analysis: Joint space limits

The dexterous and rotational workspaces for the RSR and HC were constructed given the joints' dimensions and constraints (Fig. 5). The HC's dexterous workspace presents a cone-like shape, and it's independent of the position and orientation of the end-effector. Whereas the RSR dexterous workspace presents a dome-like shape and it's dependent on the position and orientation of the mechanism end-effector. Furthermore, the theoretical rotational workspace of RSR presents a diamond-like structure, whereas sigma.7 is based on a serial arm, so it is a grid-like structure with the following limits ($235^\circ \times 140^\circ \times 200^\circ$). The kinematic analysis illustrates the kinematic dissimilarities between the HC controller and RSR, where each structure presents a unique operational dexterous and rotational workspace. Also, the RSR operational dexterous and rotational workspaces change as a function of end effector position and orientation, whereas the HC workspaces remain unchanged due to the hybrid nature of the HC mechanism.

5. VIRTUAL ROBOT SIMULATION AND ANALYSIS

To verify the kinematics of the RSR mechanism and input-output relationship, we develop a virtual RSR using the Gazebo simulator. The robot was represented in the simulator by dividing its components into different links (L1-L5) and connecting them through joints (J.Ai-Di), following the parent-child convention to establish the link-joint relationship. This resulted in a closed-loop link-joint relationship in Gazebo that closely resembled the real-world configuration of the RSR. A simulation inside the Gazebo simulator was performed to determine the RSR end effector deviation from the input desired path.

During the simulation, a sinusoidal path with varying periods for each axis was input as the desired path for RSR to follow for all 6-DOF (translation and rotation) (video attached). During the simulation, the lengths of the linear actuators and the angles of the active joints' were calculated and interfaced with the RSR in the Gazebo simulator

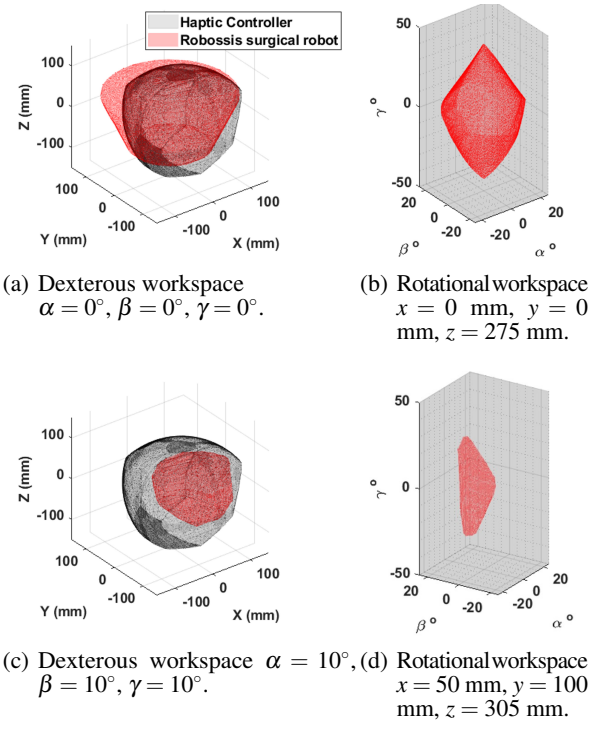

(a) Dexterous workspace $\alpha = 0^\circ, \beta = 0^\circ, \gamma = 0^\circ$.

(b) Rotational workspace $x = 0$ mm, $y = 0$ mm, $z = 275$ mm.

(c) Dexterous workspace $\alpha = 10^\circ, \beta = 10^\circ, \gamma = 10^\circ$.

(d) Rotational workspace $x = 50$ mm, $y = 100$ mm, $z = 305$ mm.

Fig. 5. Theoretical simulation of the HC and RSR operational workspace for the dexterous and rotational workspace. (a) shows the dexterous workspace of RSR and HC at constant orientation of the end effector. (b) demonstrate the rotational workspace of RSR and HC at constant position of the end effector. (c) and (d) present the dexterous and rotational workspace at a different position and orientation of the end effector. The RSR operational dexterous and rotational workspaces change as a function of the end effector position and orientation whereas the HC remains unchanged due to the hybrid nature of the HC mechanism. The rotational workspace for sigma.7 is based on a serial arm, so it is a grid-like structure with the following limits ($235^\circ \times 140^\circ \times 200^\circ$).

using a custom model plugin. Fig. 6 displays the desired and measured input path for translation (Fig. 6(a)) and rotation (Fig. 6(b)), as well as the corresponding error observed during the simulation (Fig. 6(c)). The maximum absolute deviation observed for the translational and rotational motion was 0.2 mm and 0.1 degrees. As such, the simulation validates the kinematics of the RSR to accurately follow a desired trajectory and defines the relationship between the users' desired motion and input trajectory.

6. MOTION TRANSFER AND CONTROL

Motion transfer and control of the RSR can be achieved with a manual graphical user interface (GUI) or real-time

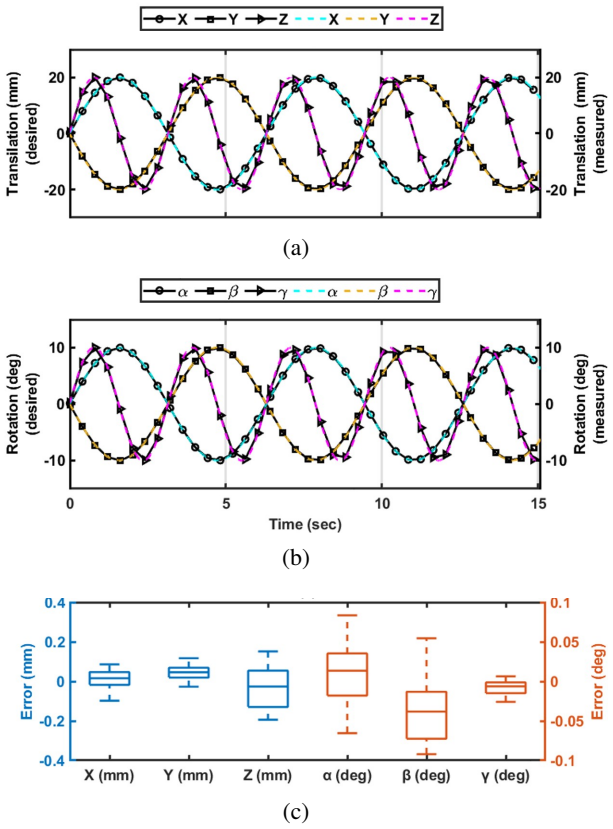

Fig. 6. Robossis surgical robot's desired trajectory as commanded a sinusoidal trajectory in 6-DOF ((a) translation and (b) rotation). (c) A maximum absolute deviation for the translational motion (0.2 mm) and rotation motion (0.1 deg) during the entire simulation.

motion via the HC (sigma.7). For manual motion, a time-controlled trajectory generation scheme is implemented using a trigonometric function as

$$x(t)_{RSR} = \begin{cases} x_0, & t < t_0, \\ x_0 + dx, & t > t_0 + dt, \\ \frac{dx}{2} * \sin\left(\frac{180}{dt} * (t - t_0) - 90\right) + x_0 + \frac{dx}{2}, \end{cases} \tag{10}$$

where x_0 is the initial position, dx is the desired change of motion, t_0 is the initial time of change, and dt is the desired time to complete the motion. The time-controlled trajectory scheme is generalized to all translational and rotational motions. Furthermore, the real-time motion integration between the HC (user's hands) and RSR is achieved as an incremental trajectory as

$$\boldsymbol{x(t)_{RSR}} = \boldsymbol{x_{RSR}(t-1)} + \boldsymbol{S} * [\boldsymbol{x(t)_{HC}} - \boldsymbol{x(t-1)_{HC}}], \tag{11}$$

where $\boldsymbol{x(t)_{RSR}} \in R^6$ and $\boldsymbol{x_{RSR}(t-1)} \in R^6$ is the current and previous location of the RSR, and $\boldsymbol{x(t)_{HC}} \in R^6$ and $\boldsymbol{x(t-1)_{HC}} \in R^6$ is the current and previous location of the HC (user's hands). Also, $\boldsymbol{S} \in R^{6x6}$ is the linear and angular dynamic scaling matrix and defined as

$$\boldsymbol{S} = \begin{bmatrix} \boldsymbol{I_{3x3}} * \frac{[Max_v]}{\|\boldsymbol{v_{HC}}\|} & 0_{3\times3} \\ 0_{3\times3} & \boldsymbol{I_{3x3}} * \frac{Max_\omega}{\|\boldsymbol{\omega_{HC}}\|} \end{bmatrix}, \tag{12}$$

where $\|\boldsymbol{v_{HC}}\|$ and $\|\boldsymbol{\omega_{HC}}\|$ is the norm of the linear and angular velocities of the HC (user's hands) during motion $\sim \dot{\boldsymbol{x}}(t)_{\boldsymbol{HC}} \in R^6$. Also, Max_v, Max_ω are the desired maximum linear and angular velocities based on the user's desired input, and $\boldsymbol{I_{n\times n}}$ is identity matrix with n rows and n columns. Additionally, the trajectories from the HC ($\boldsymbol{x(t)_{HC}}$) are collected at a sampling rate of 1 kHz, due to the communication protocol (USB – connection), which does not meet the required sampling rate to actuate the RSR stepper motors. Given this, the incremental trajectory of the RSR ($\boldsymbol{x(t)_{RSR}}$) is up-sampled using linear interpolation. After, we implement the Kalman filter to predict the future state of the RSR where the hidden states of trajectories are continuous (i.e., velocity, and acceleration). In our approach, we infer the hidden states of RSR (velocity and acceleration) from the observable state, i.e., position trajectory. The Kalman filter can be modeled as

$$\boldsymbol{x(t)_{RSR,U}} = \boldsymbol{x(t)_{RSR,p}} + \boldsymbol{K(t)} * [\boldsymbol{x(t)_{RSR}} - \boldsymbol{H x(t)_{RSR,P}}], \tag{13}$$

where $\boldsymbol{x(t)_{RSR,P}} \in \boldsymbol{R^6}$ is the predicted observable state, $\boldsymbol{x(t)_{RSR}} \in \boldsymbol{R^6}$ observations, $\boldsymbol{H} \in \boldsymbol{I_{6\times6}}$ is the observation matrix, $\boldsymbol{x(t+1)_{RSR,U}} \in I_{6x6}$ is the updated state estimate. Also, $\boldsymbol{k(t)}$ is the Kalman gain and can be estimated as

$$\boldsymbol{k(t)} = \boldsymbol{P_{RSR,p}(t)H^T} * [\boldsymbol{H P_{RSR,p}(t) H^T} + \boldsymbol{N}]^{-1}, \tag{14}$$

where $\boldsymbol{P_{RSR,p}(t)} \in \boldsymbol{R^{6\times6}}$ and $\boldsymbol{N} \in [100000 * I_{6\times6}]$ are the predicted covariance and noise covariance matrix, respectively. The noise covariance matrix $\boldsymbol{N}$ is experimentally determined to generate a stable trajectory for the RSR.

Fig. 7 illustrates the analysis of the motion integration approach proposed in this paper. The HC (hand-motion) trajectory shows a breakage in position, velocity, and acceleration (Figs. 7(a)-7(c)). The high velocity and acceleration in the raw trajectory are due to the breakage in the position profile and the loss of communication between the HC and control software. We implement two cycles of moving average filter, once before the up-sampling and once before the Kalman filter, to smooth the hidden state of the trajectories. After processing, we are able to generate a trajectory that is continuous for the position, velocity, and acceleration (Figs. 7(a), 7(d), and 7(e)). Also, the trajectory hidden state (i.e., the velocity profile) is capped for the different case sceneries at 10 $\frac{\text{mm}}{\text{sec}}$, 5 $\frac{\text{mm}}{\text{sec}}$, and 2 $\frac{\text{mm}}{\text{sec}}$ (for demonstration purposes only, in the actual setting, the speed is at 2 mm/sec) despite

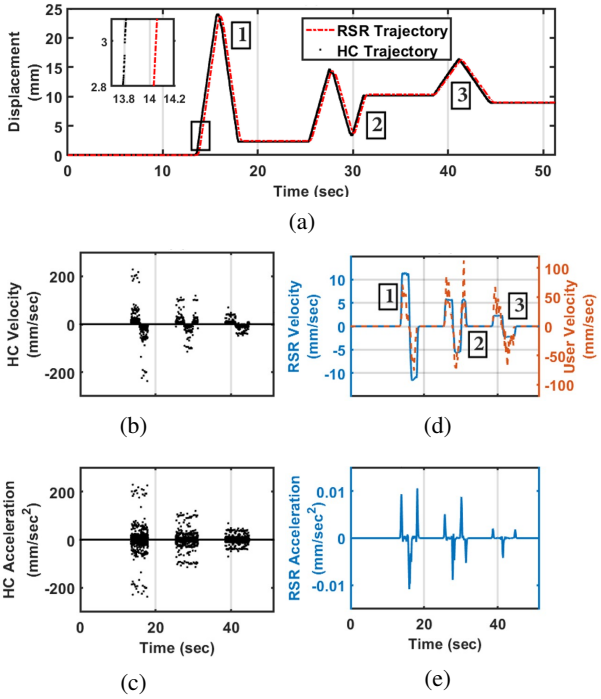

Fig. 7. Analysis of the motions control approach. The input trajectory from the HC has a breakage in position, velocity, and acceleration. (a) shows the position profile from the HC and RSR desired trajectory at a different speed as set by the user. (b) and (c) show the instantaneous velocity and acceleration profile for the original raw HC trajectory where there is a breakage in position, velocity, and acceleration. (d) and (e) show the instantaneous velocity and acceleration profile for the RSR where the trajectory is continuous in position, velocity, and acceleration. (d)-right axis shows the user speed moving freely for the different case sceneries, despite, the RSR trajectories are scaled to meet the maximum desired speed as set by the user. For each case scenario 1, 2, and 3, the maximum speeds set by the user were 10 mm/sec, 5 mm/sec, and 2 mm/sec, respectively. Implementation of the proposed approach results in a smooth and continuous position, velocity, and acceleration trajectory as input to the RSR.

the user velocity (user's hand speed) moving freely at a speed of $\sim$ 0-100 mm/sec (Fig. 7(d)-right axis). The user is able to dynamically set the desired maximum linear and angular velocity using a developed guided user interface (GUI).

6.1. Motor actuation

The joint velocity of the Robossis surgical robot is a 6×1 vector denoting the three rotatory and linear actuators, respectively

$$\dot{\boldsymbol{q}}_{RSR} = [\dot{\theta}_1 \ \dot{\theta}_2 \ \dot{\theta}_3 \ \dot{d}_1 \ \dot{d}_2 \ \dot{d}_3]^T. \tag{15}$$

The linear and angular velocities of the moving platform are defined to be v and ω, respectively. Thus, $\dot{x}_{RSR} \in \boldsymbol{R}^6$ can be written as a velocity vector

$$\dot{\boldsymbol{x}}_{\boldsymbol{RSR}} = [\boldsymbol{v}_{\boldsymbol{RSR}} \ \boldsymbol{\omega}_{\boldsymbol{RSR}}]. \tag{16}$$

The Jacobian matrix relates $\dot{q}_{RSR}$ and $\dot{x}_{RSR}$ as follows:

$$\dot{\boldsymbol{q}}_{\boldsymbol{RSR}} = J\dot{\boldsymbol{x}}_{\boldsymbol{RSR}}. \tag{17}$$

The concept of reciprocal screws is applied to derive J. As such, the angular velocity of each joint is determined to derive the corresponding actuator pulses. By definition, the number and frequency of the pulses for each motor are proportional to the angular velocity of the joints. We use the Euler backward numerical approximation to estimate the number of revolutions for each ith motor and, hence, determine the number of pulses to actuate each motor

$$q(n)_{RSR,i} = q(n-1)_{RSR,i} + k * [t(n) - t(n-1)] * \dot{q}(n)_{RSR,i}, \tag{18}$$

$$Pulses = \begin{cases} 1, & \sin(q(n)_{RSR,i}) > 0, \\ 0, & \sin(q(n)_{RSR,i}) < 0, \end{cases} \tag{19}$$

where k is the gain constant that is a property of each motor. The RSR motors are a five-phase stepper with a 0.72 step angle, so for one complete revolution of the shaft, there are 500 pulses, and this is equivalent to the k constant.

7. HAPTIC 6-DOF JOINT SPACE RENDERING

Due to the nature of the RSR parallel mechanism and coupling between the translational and rotational workspaces, the allowable workspace of the RSR changes with respect to the end effector position and orientation. Addressing this complexity requires an approach that can dynamically approximate the forbidden region for the follower robot end-effector task space and, therefore, estimate the required haptic information that reshapes the user input motion within these allowable limits. As such and to account for the kinematic mismatch, a haptic rendering pipeline is proposed. The haptic rendering pipeline restricts the movement of the haptic controller inside the changing virtual workspace of the RSR based on the physical constraints of the structure (Fig. 8).

7.1. Haptic rendering pipeline

The haptic feedback imposed on the user's hand is modeled as a spring-damping system

$$\boldsymbol{F}_{\boldsymbol{wall}} = -k_{\boldsymbol{f}} * \|d\| * \widehat{\boldsymbol{n}} - c_{\boldsymbol{f}} * \boldsymbol{v}_{\boldsymbol{HC}}, \tag{20}$$

$$\boldsymbol{\tau}_{\boldsymbol{wall}} = -k_{\boldsymbol{\tau}} * \|d\| * \widehat{\boldsymbol{n}} - c_{\boldsymbol{\tau}} * \boldsymbol{\omega}_{\boldsymbol{HC}}, \tag{21}$$

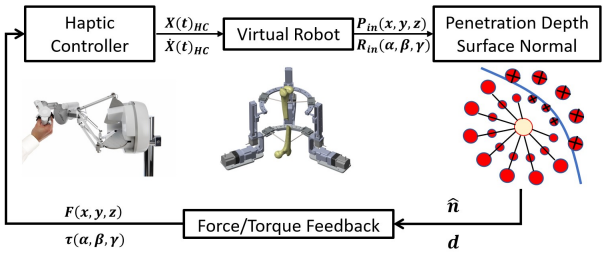

Fig. 8. Haptic rendering pipeline. The method used to render the motion of the HC within the RSR joint space limits. The haptic rendering pipeline restricts the movement of the HC inside the virtual workspace of the RSR which changes based on the orientation and position of the RSR end-effector. The end effector is encapsulated by two spherical point clouds, a translational and a rotational spherical point cloud, with radii 15 mm and 5°, respectively. When any of the points in these two spheres are outside the RSR joint space limits, the movement of the HC is restricted via haptic force feedback.

where $\boldsymbol{F_{wall}} \in R^3$ and $\boldsymbol{\tau_{wall}} \in R^3$ are the force and torque vectors inserted at the contact of the virtual wall, respectively. Also, $\|\boldsymbol{d}\|$ is the modeled sphere interaction to the forbidden region of the RSR workspace, $\hat{\boldsymbol{n}}$ is the unit vector that approximates the direction of the haptic information; $\boldsymbol{v_{HC}}$ and $\boldsymbol{\omega_{HC}}$ are the linear and angular velocity vectors of the HC, respectively; c_f and c_τ are the damping constant (15 N s/m and 0.001 Nm s/deg); and k_f and k_τ are the spring constant (2000 N/m and 0.12 Nm/deg). $\|\boldsymbol{d}\| \in R^2$ and $\hat{\boldsymbol{n}} \in R^{2\times 3}$ can be estimated as

$$\|\boldsymbol{d}\| = \begin{bmatrix} \left\| \boldsymbol{X}(t)_{HC,xyz} - \frac{\sum^n \boldsymbol{P_{in}}(xyz)}{n} \right\| \\ \left\| \boldsymbol{X}(t)_{HC,\alpha\beta\gamma} - \frac{\sum^n \boldsymbol{R_{in}}(\alpha\beta\gamma)}{n} \right\| \end{bmatrix}, \tag{22}$$

$$\hat{\boldsymbol{n}} = \frac{\boldsymbol{d}}{\|\boldsymbol{d}\|}, \tag{23}$$

where $\frac{\sum^n \boldsymbol{P_{in}}(xyz)}{n}$, $\frac{\sum^n \boldsymbol{R_{in}}(\alpha\beta\gamma)}{n}$ are the mean of the point clouds remaining inside the operational workspace of the RSR. The end effector of the HC is encapsulated by two spherical point clouds (100 points), a translational $\boldsymbol{P_{in}}(\boldsymbol{xyz})$ and a rotational $\boldsymbol{R_{in}}(\boldsymbol{\alpha\beta\gamma})$ spherical point cloud, with radii 15 mm and 5°, respectively. To ensure evenly distributed points on the surface of the sphere, we generate the points following the Fibonacci method on the surface of the sphere, i.e., the golden angle distribution [33]. When any of the points in these two spheres are outside the RSR joint space limits, the movement of the HC is restricted via haptic force feedback. We implement parallel computing to determine the point clouds that are inside/outside the operational limits of the RSR workspace. As such, with this implementation, the computation cost of the haptic rendering is minimized and designed to meet the required 1 kHz haptic update loop

Algorithm 1: Haptic rendering pipeline.

Haptic rendering pipeline
Input: Haptic controller→ $\boldsymbol{X}(\boldsymbol{t})_{\boldsymbol{HC}} \in \boldsymbol{R^6}$
Outpoints→[]
For →N # of point clouds (PC)
  flag → Virtual Robot InvKinematics($\boldsymbol{X}(\boldsymbol{t})_{\boldsymbol{HC}} + \boldsymbol{PC}(\boldsymbol{N})$)
  If flag → True (*True if* $(\boldsymbol{X}(\boldsymbol{t})_{\boldsymbol{HC}} + PC(N))$ *is outside*)
    Outpoints → $((\boldsymbol{X}(\boldsymbol{t})_{\boldsymbol{HC}} + \boldsymbol{PC}(\boldsymbol{N}))) \in \boldsymbol{R^6}$
  Else
    $\boldsymbol{P_{in}}(\boldsymbol{xyz}) \rightarrow (\boldsymbol{X}(\boldsymbol{t})_{\boldsymbol{HC,xyz}} + \boldsymbol{PC}(\boldsymbol{N})) \in \boldsymbol{R^3}$
    $\boldsymbol{R_{in}}(\boldsymbol{\alpha\beta\gamma}) \rightarrow (\boldsymbol{X}(\boldsymbol{t})_{\boldsymbol{HC,\alpha\beta\gamma}} + \boldsymbol{PC}(\boldsymbol{N})) \in \boldsymbol{R^3}$
  End
End
If *Outpoints.Length()* > 0
  Penetration Depth Norm → (22) $\in \boldsymbol{R^2}$ (averaged)
  Direction of Force/Torque → (23) $\in \boldsymbol{R^{2\times 3}}$
  FX, **FY**, **FZ** → (20) $\in \boldsymbol{R^3}$ *(mean weighted)*
  T$\boldsymbol{\alpha}$, **T**$\boldsymbol{\beta}$, **T**$\boldsymbol{\gamma}$ → (21) $\in \boldsymbol{R^3}$ *(mean weighted)*
Else
  FX, **FY**, **FZ** → $-\boldsymbol{c_f} * \boldsymbol{v_{HC}} \in \boldsymbol{R^3}$ *(damping force)*
  T$\boldsymbol{\alpha}$, **T**$\boldsymbol{\beta}$, **T**$\boldsymbol{\gamma}$ → $-\boldsymbol{c_\tau} * \boldsymbol{\omega_{HC}} \in \boldsymbol{R^3}$ *(damping force)*
End
Output: Force & Torque Projected on the Haptic Controller

[34].

Furthermore, we implement a moving average (window of 20) on the modeled interaction ($\|\boldsymbol{d}\|$), and a mean weighted (window of 20) on the forces and torques to account for the sharp changes in the surface and stability of the haptic feedback. Algorithm 1 shows the overall pseudocode for the haptic rendering pipeline. The input from the HC includes the mapped translation and rotation location of the end effector. Then, a check for all the point clouds determines if the points are inside or outside the operational workspace while implementing the parallel computing to optimize the run time for the computation. Furthermore, if any of the point clouds are outside the workspace, the pipeline imposes haptic feedback on the user's hands.

7.2. Haptic feedback analysis

A simulation study was completed to analyze the haptic feedback magnitude and direction at the edges of the workspace. The simulation was completed by moving the end effector of the RSR into the edges of the workspace and collecting the haptic feedback responses. Fig. 9 shows the magnitude of the forces and torques as the haptic end-effector penetrates the surfaces of the RSR's dexterous and rotational workspaces, where it was at a maximum at the edge of the boundary. The force feedback analysis shows the magnitude of the force and torque increases to a maximum (15 N and 0.3 Nm) at the edge of the boundary. Also,

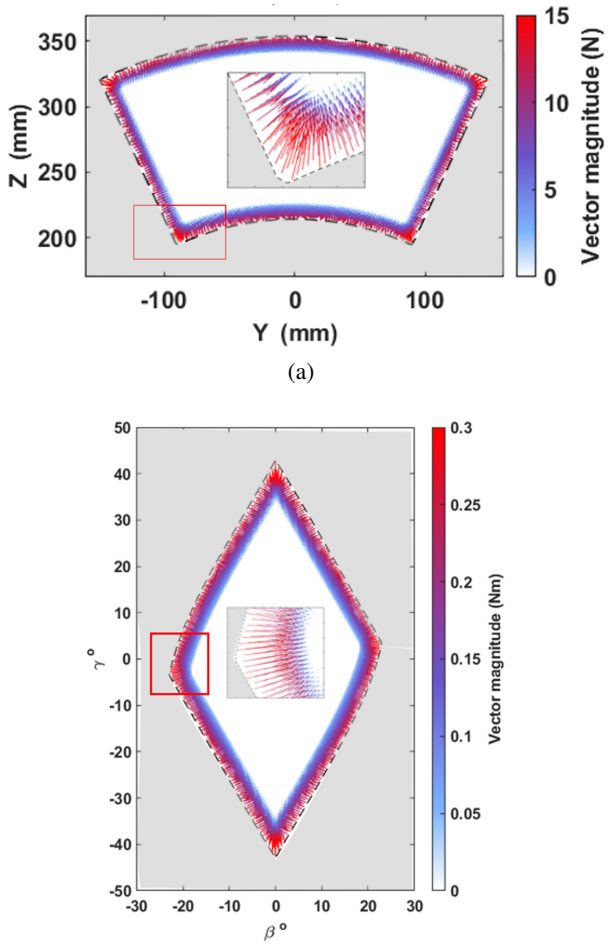

Fig. 9. Force feedback analysis shows the magnitude of the force and torque increases to a maximum at the edge of the boundary. The haptic feedback is normal to the penetrating vectors, with increasing forces (a) and torques (b) as the end effector reaches the boundary (dashed-black line).

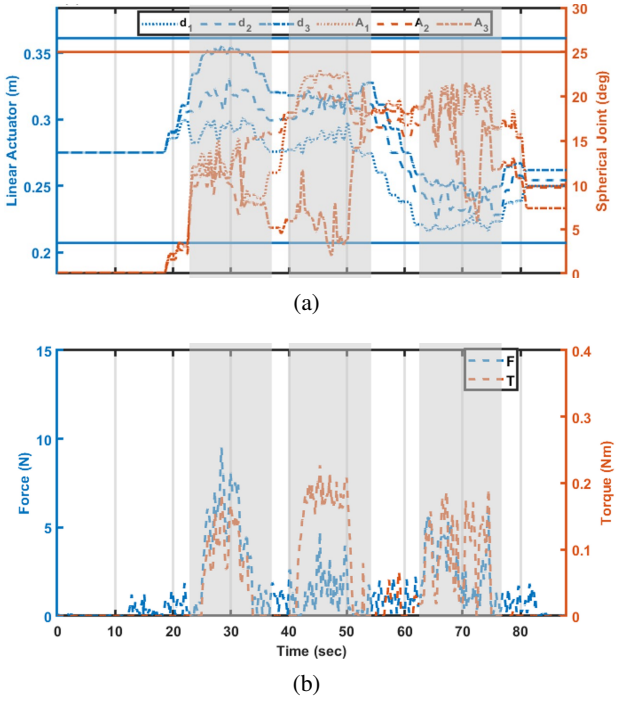

Fig. 10. (a) As the user manipulates the haptic controller and reaches the limits of linear actuator (0.214 m-0.354 m) and spherical joints ($\pm 25°$), (b) haptic feedback is projected into the user's hand to keep the user's hand within the limit of RSR joints. If the user was forcing the HC to exceed the maximum limits of the workspace, 15 N and 0.3 Nm were the maximum haptic feedback would be experienced during the simulation from the HC. When the user is not in a collision with the surfaces, a viscous force is projected onto the user hand. The user maximum speed while interacting with the haptic surfaces was 10 mm/sec and 1 deg/sec.

haptic feedback is modeled as a gradual haptic increase as the motion approaches the boundary of the workspace. The haptic feedback is normal to the penetrating vectors, with increasing forces and torques as the end effector reaches the boundary.

Furthermore, an additional study was completed where the user was tasked to move in the workspace of the RSR. Fig. 10 shows the forces and torque feedback analysis of the haptic rendering pipeline. Overall, as the user manipulates the haptic controller and reaches the limits of the linear actuator (d_i) (0.284 ± 0.07) m and or spherical joints ($\pm 25°$), haptic feedback is projected into the user's hand to keep the user's hand within the limit of the workspace. If the user was forcing the HC to exceed the maximum limits of the workspace, 15 N and 0.3 Nm were the maximum haptic feedback would be experienced during the simulation from the HC (75% of the maximum forces and torques of the sigma.7 HC). Also, the computational cost of the haptic rendering pipeline during the simulation is analyzed. The result shows that the haptic rendering pipeline can meet the required 1 kHz haptic update loop during the simulation.

8. EXPERIMENTAL TESTING AND RESULTS

The Robossis system was tested in a benchtop and cadaver lab as a proof of concept. Fig. 11 shows the Robossis system, which consists of a haptic unit, a surgical unit, and the different components of the system, including sigma.7, RSR, hardware/software, and the optical tracking system (Optitrack Flex 13, residual within ± 0.08 mm and $\pm 0.03°$, NaturalPoint, Inc. DPA OptiTrack). Optitrack's motion capture cameras and Motive software were used to track the

6-DOF motion of RSR during the experimental testing. To track the end effectors of the RSR, markers were placed in a specific location and orientation on the moving rings and three Optitrack cameras were placed above RSR to capture movements.

8.1. Real-time motion analysis

Real-time motion testing of the Robossis system is completed to determine the system's accuracy when moving to different locations in the operational workspace using the GUI and HC. During testing, the RSR was tasked to follow the motion of the user's hand and manual motion. The theoretical trajectories from the HC (user's hand) and manual motion (GUI) were recorded and synced with the RSR actual trajectory (optical tracking software) (Fig. 12). Fig. 12 shows the motion testing procedure trajectories for the translational and rotational motion while synced with the absolute error throughout the entire testing. The results in Fig. 12 show that RSR can follow the motion of the desired trajectory while maintaining a minimal deviation. Error analysis (Fig. 12) shows an average translational, and rotational error of 0.32 mm and 0.07° between the RSR actual trajectory and HC-GUI desired trajectory. Maximum translational and rotational errors of 1.8 mm and 0.27° were observed in the z-direction and γ-direction, respectively.

8.2. Cadaver lab testing

In a cadaveric lab, the Robossis system was used to assist surgeons during a mock femur fracture surgery. Fig. 13(a) shows the cadaver lab setup, which includes the HC, RSR, and the cadaver patient attached to the RSR. During the mock surgery, the patient's femur was cut using a reciprocating saw to represent a midshaft femur fracture. The distal fragment was attached to the RSR moving ring, and the proximal fragment was clamped down to eliminate

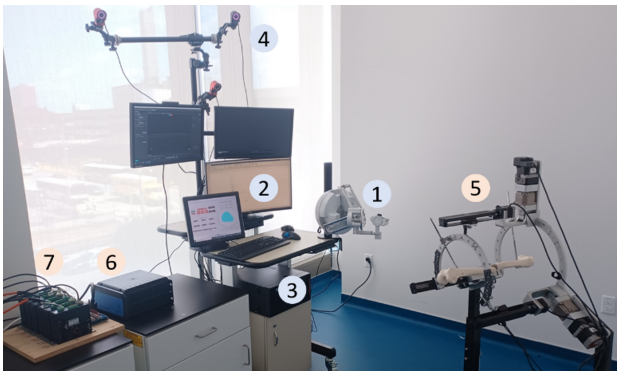

Fig. 11. Robossis system. The haptic unit includes ① the haptic sigma.7, ② screen monitors, ③ the haptic unit PC, and ④ the Optitrack optical trackers. The surgical unit includes ⑤ Robossis surgical robot, ⑥ the surgical unit PC (Speedgoat, Mathworks - Switzerland), and ⑦ motor drivers.

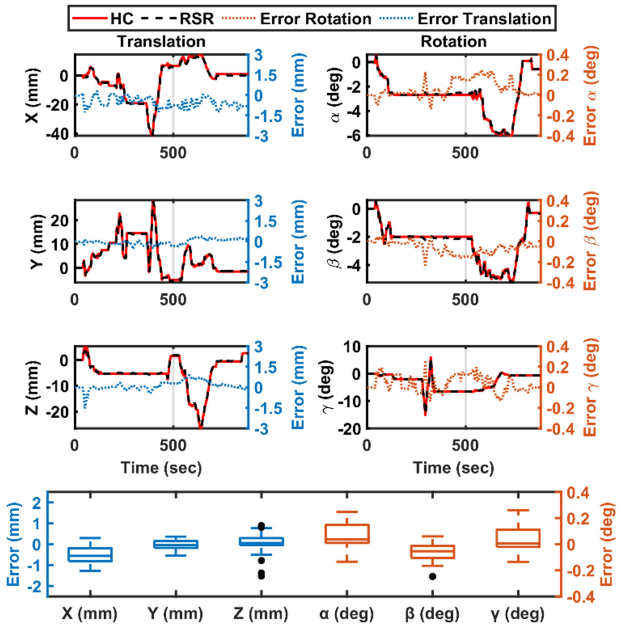

Fig. 12. Trajectory comparison between the RSR actual trajectory (Optitrack) and theoretical trajectory from the HC and GUI. The motion testing procedure trajectories for the translational and rotational motion were synced with the absolute error throughout the entire testing. The box and whisker plot shows an average translational, and rotational error of 0.32 mm and 0.07° between the RSR actual trajectory and HC-GUI desired trajectory.

movement. The orthopedic surgeons utilized the Robossis system to manipulate the RSR. Throughout the surgical procedure, the surgeons completed varying maneuvers to assess the Robossis system load-holding capacity (muscle traction forces) and usability in the clinical setting. The results showed that Robossis was able to assist the surgeon in performing femur fracture surgery and aligning the broken femur fragments (Figs. 13(b) and 13(c)). In addition, the RSR was able to counteract the actual physiological muscle traction forces while manipulating the distal bone fragments during the surgery. In [18], we present a clear description of the cadaver lab experimental testing as assisted by the novel imaging software. Lastly, the surgeons were able to conclude that the Robossis system able to provide an intuitive solution for surgeons to perform surgery.

9. DISCUSSION

The outcome of this study demonstrates the development of the leader-follower Robossis system that is designed to assist surgeons during femur fracture surgery. Considering the Robossis system in the application of femur fractures, the surgical robot needs to be highly maneuverable, insert the required forces, and have highly accurate manipulation.

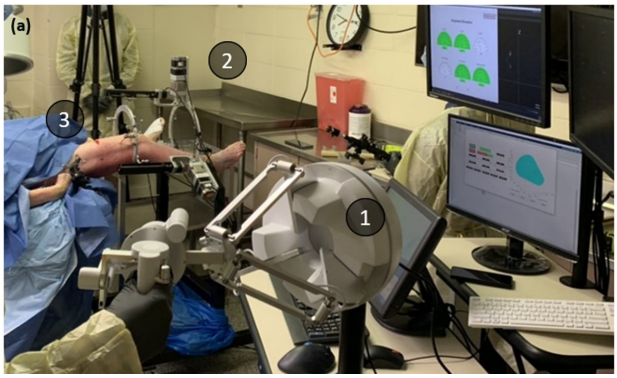

(a)

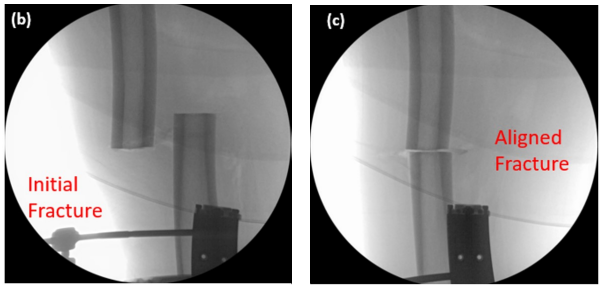

(b) (c)

Fig. 13. (a) Robossis system was used to assist the orthopedic surgeons during a cadaveric femur fracture surgery where ① the haptic sigma.7, ② the RSR attached to the cadaver patient ③. (b) shows the femur pre-fractured location of the bone. (c) shows the aligned fracture using the Robossis system.

In previous work [16], we performed a kinematic comparison between the RSR and the well-known Gough-Stewart platform to evaluate their ability to meet the required alignment ranges. Our results demonstrate that the RSR can achieve the femur fracture malalignment ranges in each axis, as previously reported in the literature, whereas the Gough-Stewart platform exhibits limited motion capability. These findings confirm the advantages of the RSR in meeting the clinical requirements for femur fracture surgeries.

Additionally, the haptic rendering pipeline is implemented to reshape the user input motion to match the RSR's operational workspace. This ensures the safety of the RSR's joints and eliminates any chances of failure during surgery. For future work, we will render muscle reaction forces to the operator interacting with the RSR. This information provides critical insight into the traction force and robot-patient interaction. Rendering muscle reaction forces is crucial as it enhances realism by simulating the forces exerted by muscles and other soft tissues, thereby reducing the risk of over-correction or causing additional trauma to the patient, such as bone-bone collision. It also ensures safety by helping to prevent excessive force application, which can lead to tissue damage. This is particularly important for the Robossis system, given its high-load insertion capabilities.

Further, the current system requires experience and training to significantly improve the standard of care for long-bone fractures. To address this, our team is developing the Robossis surgical simulator to enable surgeons to feasibly train and master the system. Within the virtual reality environment, we have created digital twins of the Robossis system to train users on how to interact with the system and understand its limits in a low-cost, low-risk setting. This implementation ensures that users transitioning to the real-world Robossis system will have the necessary knowledge and skills to operate the system effectively and safely.

For future work, we plan to optimize the Robossis system and overcome the limitations presented in the current study. Optimization of the hardware of the robot and structure will be performed to meet a wide range of patient sizes and weights. We recognize the limitations of using a single cadaver and plan to expand our testing to include a larger sample size and a variety of fracture types in future work. This will aid in the identification of potential risks, limitations, and long-term use considerations associated with the proposed system. Additionally, we will optimize the Robossis system control architecture to include a bilateral control framework with advanced control methods [35]. This will create a transparent system that can meet the demands of the user experience and clinical requirements. We will also explore extending the Robossis system into different surgical applications.

10. CONCLUSION

To successfully restore the length, alignment, and rotation of the fractured femur, the femur fragments must be manipulated and returned to their correct anatomical position. All of this must be done while the surgeon is exerting large traction forces and torques (517 N and 74 N·m). In this study, we have been able to present the development of the leader-follower Robossis system for femur fracture surgery that includes the design of an architecture that addresses 1) the kinematic mismatch and 2) real-time motion transfer between the HC and RSR. The feasibility of the Robossis system was experimentally evaluated through a benchtop and cadaveric experiment. Through experimental testing and clinician feedback, we demonstrated that the system has the potential for clinical use to improve the quality of fracture reduction.

CONFLICT OF INTEREST

The authors declare that they have no conflict of interest.

REFERENCES

[1] S. Hwang, S. Lee, and S. Kim, "Surgical navigation system for pedicle screw placement based on mixed reality," *International Journal of Control, Automation, and Systems*, vol. 21, no. 12, pp. 3983-3993, 2023.

[2] S.-W. Bang, Y.-J. Lee, H. Kee, and S. Park, "Registration-free minimally invasive surgery without preoperative phase," *International Journal of Control, Automation, and Systems*, vol. 21, no. 10, pp. 3313-3323, 2023.

[3] D.-H. Lee, K.-S. Kwak, and S.-C. Lim, "A neural network-based suture-tension estimation method using spatio-temporal features of visual information and robot-state information for robot-assisted surgery," *International Journal of Control, Automation, and Systems*, vol. 21, pp. 4032-4030, 2023.

[4] J. X. Zhao, C. Li, H. Ren, M. Hao, L. C. Zhang, and P. F. Tang, "Evolution and current applications of robot-assisted fracture reduction: A comprehensive review," *Annals of Biomedical Engineering*, vol. 48, no. 1, pp. 203-224, 2020.

[5] L. Bai, J. Yang, X. Chen, Y. Sun, and X. Li, "Medical robotics in bone fracture reduction surgery: A review," *Sensors*, vol. 19, no. 16, 3593, 2019.

[6] Q. Zhu, B. Liang, X. Wang, X. Sun, and L. Wang, "Force-torque intraoperative measurements for femoral shaft fracture reduction," *Computer Assisted Surgery*, vol. 21, pp. 37-45, 2016.

[7] T. Gösling, R. Westphal, J. Faülstich, K. Sommer, F. Wahl, C. Krettek, and T. Hufner, "Forces and torques during fracture reduction: Intraoperative measurements in the femur," *Journal of Orthopaedic Research*, vol. 24, no. 3, pp. 333-338, 2006.

[8] C. K. Yu, V. A. Singh, S. Mariapan, and S. T. B. Chong, "Antegrade versus retrograde locked intramedullary nailing for femoral fractures: Which is better?," *European Journal of Trauma and Emergency Surgery*, vol. 33, no. 2, pp. 135-140, 2007.

[9] C. Li, T. Wang, L. Hu, P. Tang, L. Wang, L. Zhang, N. Guo, and Y. Tan, "A novel master-slave teleoperation robot system for diaphyseal fracture reduction: A preliminary study," *Computer Assisted Surgery*, vol. 21, pp. 163-168, 2016.

[10] M. X. Kong, Z. J. Du, L. N. Sun, L. X. Fu, Z. H. Jia, and D. M. Wu, "A robot-assisted orthopedic telesurgery system," *Proc. of Annual International Conference of the IEEE Engineering in Medicine and Biology*, Institute of Electrical and Electronics Engineers Inc., pp. 97-101, 2005.

[11] M. H. Abedinnasab, Y.-J. Yoon, and H. Zohoor, "Exploiting higher kinematic performance-Using a 4-legged redundant PM rather than Gough-Stewart platforms," *Serial and Parallel Robot Manipulators-Kinematics, Dynamics, Control and Optimization*, vol. 10, 32141, 2012.

[12] R. Westphal, S. Winkelbach, F. Wahl, T. Gösling, M. Oszwald, T. Hüfner, and C. Kerttek, "Robot-assisted long bone fracture reduction," *The International Journal of Robotics Research*, vol. 28, no. 10, pp. 1259-1278, 2009.

[13] M. H. Abedinnasab, F. Farahmand, and J. Gallardo-Alvarado, "The wide-open three-legged parallel robot for long-bone fracture reduction," *Journal of Mechanisms and Robotics*, vol. 9, no. 1, 015001, February 2017.

[14] M. H. Abedinnasab, F. Farahmand, B. Tarvirdizadeh, H. Zohoor, and J. Gallardo-Alvarado, "Kinematic effects of number of legs in 6-DOF UPS parallel mechanisms," *Robotica*, vol. 35, no. 12, pp. 2257-2277, 2017.

[15] F. Alruwaili, M. S. Saeedi-Hosseiny, M. Clancy, S. McMillan, I. I. Iordachita, and M. H. Abedin-Nasab, "Experimental evaluation of a 3-armed 6-DOF parallel robot for femur fracture surgery," *Journal of Medical Robotics Research*, vol. 7, no. 4, 2241009, February 2022.

[16] M. Clancy, F. Alruwaili, M. S. Saeedi-Hosseiny, S. McMillan, I. I. Iordachita, and M. H. Abedin-Nasab, "Analysis and optimization of a 6-DoF 3-RRPS parallel mechanism for robot-assisted long-bone fracture surgery," *Journal of Mechanisms and Robotics*, vol. 16, no. 6, 2024.

[17] M. S. Saeedi-Hosseiny, F. Alruwaili, S. McMillan, I. Iordachita, and M. H. Abedin-Nasab, "A surgical robotic system for long-bone fracture alignment: Prototyping and cadaver study," *IEEE Transactions on Medical Robotics and Bionics*, vol. 4, no. 1, pp. 172-182, February 2022.

[18] M. S. Saeedi-Hosseiny, F. Alruwaili, M. P. Clancy, E. A. Corson, S. McMillan, C. Papachristou, N. C. Bouaynaya, I. I. Iordachita, and M. H. Abedin-Nasab, "Automatic alignment of fractured femur: Integration of robot and optical tracking system," *IEEE Robotics and Automation Letters*, vol. 8, no. 5, pp. 2438-2445, 2023.

[19] H. Alemzadeh, J. Raman, N. Leveson, Z. Kalbarczyk, and R. K. Iyer, "Adverse events in robotic surgery: A retrospective study of 14 years of FDA data," *PLoS One*, vol. 11, no. 4, e0151470, 2016.

[20] Y. Nakamura, H. Hanafusa, and T. Yoshikawa, "Task-priority based redundancy control of robot manipulators," *The International Journal of Robotics Research*, vol. 6, no. 2, pp. 3-15, 1987.

[21] G. D. Niemeyer, W. C. Nowlin, and G. S. Guthart, "Alignment of master and slave in a minimally invasive surgical apparatus," Google Patents, April 2, 2002.

[22] A. Atawnih, D. Papageorgiou, and Z. Doulgeri, "Kinematic control of redundant robots with guaranteed joint limit avoidance," *Robotics and Autonomous Systems*, vol. 79, pp. 122-131, 2016.

[23] N. Turro and O. Khatib, "Haptically augmented teleoperation," *Experimental Robotics VII*, Springer, pp. 1-10, 2001.

[24] M. Selvaggio, F. Abi-Farraj, C. Pacchierotti, P. R. Giordano, and B. Siciliano, "Haptic-based shared-control methods for a dual-arm system," *IEEE Robotics and Automation Letters*, vol. 3, no. 4, pp. 4249-4256, 2018.

[25] D. Nicolis, A. M. Zanchettin, and P. Rocco, "A hierarchical optimization approach to robot teleoperation and virtual fixtures rendering," *IFAC-PapersOnLine*, vol. 50, no. 1, pp. 5672-5679, 2017.

[26] Y. Cai, P. Choi, C.-W. V. Hui, R. H. Taylor, and K. W. S. Au, "A task space virtual fixture architecture for teleoperated surgical system with slave joint limit constraints," *IEEE/ASME Transactions on Mechatronics*, vol. 27, no. 1, pp. 69-80, 2021.

[27] Z. Li, H. Wei, C. Liu, H. Zhang, and G. Liu, "A variable admittance control strategy for robotic constraints avoidance based on virtual fixtures," *Proc. of 2023 IEEE International Conference on Robotics and Biomimetics (ROBIO)*, IEEE, pp. 1-6, 2023.

[28] A. Tobergte and P. Helmer, "A disturbance observer for the sigma. 7 haptic device," *Proc. of 2013 IEEE/RSJ International Conference on Intelligent Robots and Systems*, IEEE, pp. 4964-496, 2013.

[29] A. Tobergte, P. Helmer, U. Hagn, P. Rouiller, S. Thielmann, S. Grange, A. Albu-Schäffer, F. Conti, and G. Hirzinger, "The sigma. 7 haptic interface for MiroSurge: A new bimanual surgical console," *Proc. of 2011 IEEE/RSJ International Conference on Intelligent Robots and Systems*, IEEE, pp. 3023-3030, 2011.

[30] N. Karbasizadeh, M. Zarei, A. Aflakian, M. T. Masouleh, and A. Kalhor, "Experimental dynamic identification and model feed-forward control of Novint Falcon haptic device," *Mechatronics*, vol. 51, pp. 19-30, May 2018.

[31] D. J. Block, M. B. Michelotti, and R. S. Sreenivas, "Application of the Novint Falcon haptic device as an actuator in real-time control," *Paladyn*, vol. 4, no. 3, April 2015.

[32] R. E. Stamper, *A Three Degree of Dreedom Parallel Manipulator with Only Translational Degrees of Dreedom*, University of Maryland, College Park, 1997.

[33] Á. González, "Measurement of areas on a sphere using Fibonacci and latitude-longitude lattices," *Mathematical Geosciences*, vol. 42, pp. 49-64, 2010.

[34] Q. Tong, Q. Wang, Y. Zhang, Y. Zhang, X. Liao, W. Wei, Y. Zhang, J. Xiao, and D. Wang, "Configuration-based optimization for virtual hand haptic simulation," *IEEE Transactions on Haptics*, vol. 15, no. 3, pp. 613-625, 2022.

[35] H. Su, W. Qi, C. Yang, J. Sandoval, G. Ferrigno, and E. De Momi, "Deep neural network approach in robot tool dynamics identification for bilateral teleoperation," *IEEE Robotics and Automation Letters*, vol. 5, no. 2, pp. 2943-2949, 2020.

Fayez H. Alruwaili received his B.S. and M.S. degrees in biomedical engineering from Wichita State University, USA, in 2018 and 2019, respectively. Also, Fayez received a Ph.D. degree in biomedical engineering from Rowan University, USA, in 2024. His research interests include surgical robotics, mechatronic systems, and haptics.

Michael P. Clancy received his B.Sc. degree in bioengineering from the University of Pittsburgh and an M.S. degree in biomedical engineering from Rowan University. His research interests include medical robotics, design and optimization of mechanisms, biomechanics, and signal processing.

Marzieh S. Saeedi-Hosseiny received her B.S. degree from College of Engineering at University of Tehran, Iran, in 2008. Also, Marzieh received a Ph.D. degree in electrical and computer engineering from Rowan University, USA, in 2024. She is a co-author of three book chapters and multiple journal and conference papers. In 2020, she participated in NSF National I-Corps Program as an entrepreneurial lead. Her research interests include machine learning, image processing, computer vision, and surgical systems.

Jacob A. Logar is a Scientist I in Research and Development, contracted by Artech to Johnson and Johnson Microbiological Quality and Sterility Assurance. He is part of the Robotics and Digital Solutions (RAD), Device Processing and Equipment Engineering Management teams. He received a bachelor's degree in biomedical engineering from Rowan University. His research interests include designing, developing and implementing devices and processes throughout the medical device industry.

Chralampos Papachristou is an associate professor of statistics at Rowan University. He holds a B.S. degree in mathematics from Aristotle University of Thessaloniki, Greece, a Ph.D. degree in statistics from The Ohio State University, and completed a postdoctoral fellowship in Human Genetics at the University of Chicago. His research interests include statistical genetics, biostatistics, and genetic epidemiology.

Christopher Haydel graduated from the University of Kansas School of Medicine in 2006. He works in Moorestown, NJ and 6 other locations and specializes in Trauma Surgery and Orthopedic Surgery.

Javad Parvizi is a board certified orthopaedic surgeon specializing in pelvis, hip, and knee reconstruction with a special interest in hip pain in young adults and joint preservation procedures. He is the director of Clinical Research at the Rothman Orthopaedics.

Iulian I. Iordachita received his M.Eng. degree in industrial robotics and a Ph.D. degree in mechanical engineering from The University of Craiova, Romania, in 1989 and 1996, respectively. In 2000, he was a Postdoctoral Fellow with the Brady Urological Institute, Johns Hopkins University, Baltimore, USA, and in 2002-2003, he was a Research Fellow with the Graduate School of Frontier Sciences, The University of Tokyo, Japan. He is currently a Research Professor in mechanical engineering and robotics at Johns Hopkins University. His research interests include medical robotics, image guided surgery (specifically microsurgery), interventional MRI, smart surgical tools, and medical instrumentation.

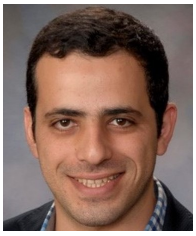

Mohammad H. Abedin-Nasab received his M.S. and Ph.D. degrees in mechanical engineering from Sharif University of Technology, in 2006 and 2012, respectively. He is currently an Assistant Professor and the Director of Surgical Robotics Lab at Rowan University in New Jersey. He is also the Editor of the Handbook of Robotic and Image-Guided Surgery. Dr. AbedinNasab specializes in surgical robotics, robotics, biomechanics, and nonlinear modeling. His research interests include both basic and applied research endeavors, ensuring that his research is consistently.